

Perturbed-angular-correlation study of phase transformations in nanoscaled Al_2O_3 -coated and noncoated ZrO_2 particles synthesized in a microwave plasma

M. Forker and J. Schmidberger

Institut für Strahlen-und Kernphysik der Universität Bonn, Nussallee 14-16, D-53115 Bonn, Germany

D. V. Szabo and D. Vollath

Institut für Materialforschung III, Forschungszentrum Karlsruhe, P.O. Box 3640, D-76021 Karlsruhe, Germany

(Received 26 July 1999)

The phase transformations of nanoscaled (n -) Al_2O_3 -coated and noncoated ZrO_2 particles synthesized in a microwave plasma have been investigated by perturbed-angular-correlation (PAC) measurements of the electric quadrupole interaction (QI) of ^{181}Ta on Zr sites between 290 and 1600 K. For the phase identification and structural characterization the QI parameters of the nanoscaled particles are compared to those of coarse-grained ZrO_2 which were measured between 290 and 2160 K. The PAC spectra of the nanoscaled particles in the as-prepared state are characterized by a broad distribution of strong, axially asymmetric QI's, which reflects a highly disordered oxygen environment of the Zr sites. Upon annealing, the tetragonal phase is the first well-crystallized structure to emerge at about 500 K, both in coated and noncoated n - ZrO_2 , in contrast to the previously reported annealing reaction of n - ZrO_2 synthesized by gas-phase condensation in which the tetragonal phase has not been observed. This disorder-order transformation is partially reversible upon cooling. In n - $\text{ZrO}_2/\text{Al}_2\text{O}_3$ synthesized in a microwave plasma the monoclinic phase can be completely suppressed up to 1600 K. In the noncoated particles monoclinic ZrO_2 starts to appear at 600 K. At 1400 K the transformation from the monoclinic to the tetragonal phase of noncoated n - ZrO_2 was observed to occur with a transformation rate of $\lambda = 6.9(1.2) \times 10^{-5} \text{ s}^{-1}$. In nanoscaled coated and noncoated tetragonal ZrO_2 the $T^{3/2}$ -temperature dependence of the quadrupole frequency ν_q is weaker than in the same phase of the coarse-grained compound, suggesting a decrease of the mean-square vibrational amplitudes with decreasing particle size.

I. INTRODUCTION

Physical properties of many materials are significantly altered by reducing the particle size below 10 nm. Therefore, nanocrystalline solids are presently under extensive investigation.¹ Because of their high potential, a large number of production processes for these materials have been developed. The comparison of different routes of synthesis for the same compound is important if the properties of nanocrystalline solids are to be tailored for specific applications. In particular, information on structure and phase stability is of interest for an evaluation of the production process.

Recently, structural properties and annealing behavior of nanocrystalline (n -) ZrO_2 prepared by inert-gas condensation have been investigated by measurements of the electric quadrupole interaction (QI) of probe nuclei on Zr sites with the perturbed-angular correlation (PAC) technique.² In the present paper these PAC studies are extended to nanoscaled zirconia produced by the microwave plasma process.^{3,4} This novel route of synthesis allows not only the production of nanoscaled ZrO_2 , but in a two-step process also allows that of nanocoated particles consisting of two different oxides in the nanoscaled core and coating.

The interaction between a nuclear electric quadrupole moment Q and the tensor of the electric-field gradient (EFG) at the nuclear site is determined by the charge distribution surrounding the probe nucleus. Because of the r^{-3} dependence of the EFG the main contribution to the QI comes from the

nearest-neighbor charges. Strength and symmetry of the QI therefore provide information on the structure of the solid on a nanometer scale and complement the structural information on nanoscaled solids obtained from scattering techniques, such as x-ray,⁵ neutron,⁶ and electron diffraction.⁴ QI parameters may serve as fingerprints for the identification of different phases of a compound. Their variation with temperature carries information on crystallization, disorder-order transformations, and phase transitions.

The perturbed-angular correlation technique is an ideal spectroscopy for the investigation of QI's in ZrO_2 ceramics because: (i) as Zr and Hf are chemically very similar, Zr compounds usually contain a Hf concentration of the order of 1–3 at. % and (ii) the β decay of 45d isotope ^{181}Hf that can be produced by thermal-neutron capture in ^{180}Hf (natural abundance 18.5 at. %) populates the 133–482 keV $\gamma\gamma$ cascade of ^{181}Ta —one of the most favorable PAC cascades with a half-life of the $I = \frac{5}{2}$ intermediate state of 10.8 nsec. Therefore in most cases Zr compounds are easily doped with the PAC probe ^{181}Ta by exposing them to a flux of thermal neutrons.

Consequently, a wide range of ZrO_2 properties has been investigated by PAC spectroscopy, such as, e.g., the monoclinic-to-tetragonal phase transition⁷ in pure ZrO_2 , oxygen diffusion^{8–11} leading to dynamic QI's, dopant stabilization of high-temperature phases,¹² the effect of ball milling,¹³ the synthesis by the sol-gel route,¹⁴ etc. The present paper describes a ^{181}Ta PAC investigation of nanoscaled ZrO_2 produced by a microwave plasma reaction. The phase transfor-

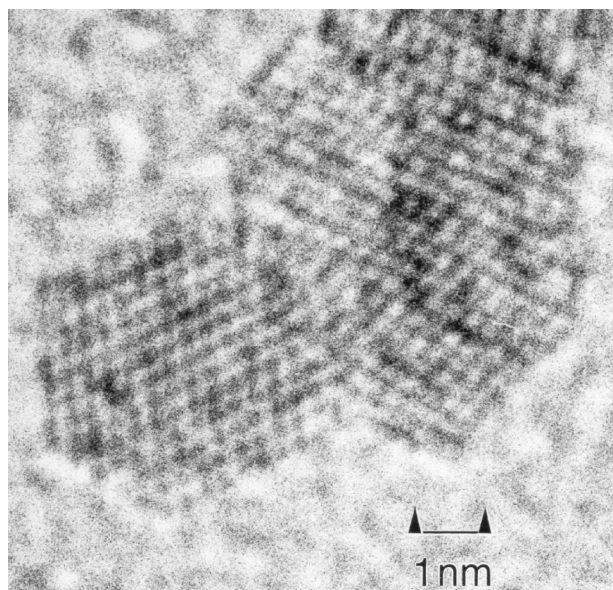


FIG. 1. Electron micrograph of a ZrO_2 particle in the as-produced state. The lattice fringes represent $\langle 111 \rangle$ planes. The fringes show a well-ordered lattice with a structure close to the fluorite structure.

mations in noncoated and Al_2O_3 -nanocoated n - ZrO_2 particles have been studied by measurement of the QI parameters at different temperatures. The QI parameters of the different phases of the coarse-grained compound have been determined between 290 and 2160 K as the base for the phase identification in nanoscaled ZrO_2 . The evolution of the phase equilibrium between the monoclinic and the tetragonal phase at elevated temperatures has been studied and the question of radiation damage related to the radioactive decay of the ^{181}Hf mother isotope has been addressed experimentally.

II. EXPERIMENTAL DETAILS

A. Sample preparation and equipment

The nanocrystalline ceramic materials investigated here were synthesized using a microwave plasma discharge—a versatile process recently developed by Vollath *et al.*^{3,4} In the case of the synthesis of an oxide, the following reaction takes place in the plasma: $MeCl_n + m/2O_2 \rightarrow MeO_m + n/2Cl_2$, where $MeCl_n = \text{AlCl}_3, \text{ZrCl}_4, \text{ or } \text{FeCl}_3$.

After forming oxide molecules by the reaction of the dissociated species, the formation of the nanoparticles is assumed to occur in the following steps: Nucleation of the particles by the random collision of two or more molecules, growth of the nuclei by further collisions with molecules, and coagulation to larger particles. By using two identical plasma stages consecutively, each one with its own supply of evaporated precursors, it is possible to produce particles consisting of an AO_n oxide core covered with a second oxide BO_m . For the present investigation noncoated pure zirconia (n - ZrO_2) and alumina-coated zirconia (n - $\text{ZrO}_2/\text{Al}_2\text{O}_3$) were produced to which we shall refer in the following as noncoated and coated n - ZrO_2 , respectively. The materials were characterized by high-resolution electron microscopy and by point analysis in a dedicated scanning-tunneling electron mi-

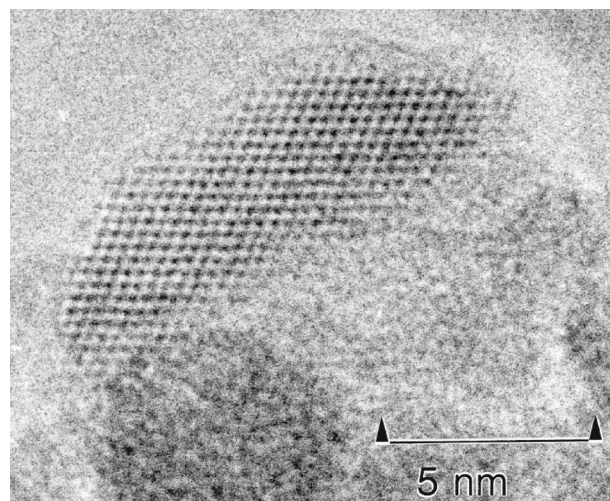


FIG. 2. Electron micrograph of an Al_2O_3 -coated ZrO_2 particle in the as-produced state. The coating is not crystallized. Therefore, it is represented by a faint halo around the particle. As in Fig. 1, the lattice fringes represent perfectly ordered $\langle 111 \rangle$ planes of a fluorite-like structure.

croscope (STEM), both combined with energy dispersive x-ray systems for microanalysis. Figure 1 shows a typical micrograph of such a material. From this micrograph it is obvious that the Zr^{4+} ions are well ordered on their lattice sites. The nanocomposite particle depicted in Fig. 2 consists of a 5–6 nm ZrO_2 core coated with an amorphous Al_2O_3 layer with a thickness of 1–2 nm. As in Fig. 1, the electron beam was parallel to the $\langle 011 \rangle$ direction of the ZrO_2 particle. The average composition of the nanocomposites was 33.9 wt. % of ZrO_2 and 66.1 wt. % of Al_2O_3 . From the electron-diffraction pattern it can be concluded that the noncoated n - ZrO_2 particles and the ZrO_2 core of the coated particles crystallize in the cubic CaF_2 structure. For the value of the lattice parameter we obtained $a = 0.506(3)$ nm. The deviations from the cubic structure are small: The evaluation of the electron-diffraction-line profile according to Dehlinger and Kochendörfer¹⁵ resulted in an average particle size of 7 nm and an isotropic lattice distortion of 2.3% for the noncoated particles. The diffraction pattern taken at 290 K remained practically unchanged after annealing for 1 h at 1100 K.

The PAC measurements were performed with the 133–482 keV $\gamma\gamma$ cascade of ^{181}Ta populated by the decay of ^{181}Hf . As pointed out in Sec. I, most Zr compounds are easily doped with ^{181}Hf by thermal-neutron irradiation. In the present investigation samples of the order of 5 mg were neutron irradiated in a flux of 5×10^{13} n/s cm^2 for 50–100 h. Before neutron activation the nanocrystalline powders were encapsulated into quartz tubes under vacuum. The activation also produces some radioactive ^{95}Zr . Its decay, however, contains only prompt coincidences and therefore affects the ^{181}Ta time spectra only close to the time zero point.

During the PAC measurements the samples were heated to a maximum temperature of 1600 K in a furnace¹⁶ designed for temperatures up to 2300 K. As a reference, coarse-grained ZrO_2 provided by Alfa Products was studied up to almost 2200 K. In this case, an open alumina boat had to be used as a sample holder. The coarse-grained material was

compacted into pellets before the neutron activation in order to avoid contamination of the furnace by ZrO_2 powder in the open boat. A few measurements on noncompacted coarse-grained zirconia encapsulated in a quartz tube were performed at $T \leq 1600$ K. Temperatures up to 1600 K were measured with a Pt-Rh-type-B thermocouple, for $T > 1600$ K we used W-Re thermocouples and a pyrometer. The PAC spectra were taken with a standard four-detector setup equipped with fast BaF_2 scintillators.

B. Data analysis

In this paper we are dealing with the static hyperfine interaction between the electric quadrupole moment Q of a nuclear state and the electric-field gradient acting at the nuclear site, which can be completely described by two independent parameters, the quadrupole frequency $\nu_q = eQV_{zz}/h$ and the asymmetry parameter $\eta = (V_{xx} - V_{yy})/V_{zz}$, where $V_{ii} = \partial^2 V / \partial x_i^2$ ($i = x, y, z$) are the principal-axes components of the EFG tensor with $|V_{xz}| \leq |V_{yy}| \leq |V_{zz}|$.

These QI parameters can be derived from the PAC spectra. Hyperfine interactions lead to a time modulation of the angular correlation coefficients A_{kk} ($k = 2, 4$) of suitable $\gamma\gamma$ cascades, which in polycrystalline samples can be described by a perturbation factor $G_{kk}(t)$. The perturbation factor depends on the multipole order, the symmetry, the time dependence of the interaction, and on the spin of the intermediate state of the cascade (for details see, e.g., Frauenfelder and Steffen¹⁷). In the present case of a static electric quadrupole interaction, the perturbation factor has the general oscillatory form:

$$G_{kk}(t; \nu_q, \eta, \delta) = s_{k0} + \sum_n s_{kn} \cos(\omega_n t) \exp[-\frac{1}{2}(\delta\omega_n t)^2]. \quad (1)$$

The hyperfine frequencies ω_n are the transition frequencies between the hyperfine levels into which the nuclear state is split by the QI. These frequencies depend on the quadrupole frequency $\nu_q = eQV_{zz}/h$ and the asymmetry parameter η . In polycrystalline samples the amplitudes s_{kn} are functions of η only. The number of terms in Eq. (1) depends on the spin of the nuclear state under consideration. The exponential factor accounts for possible distributions of the QI caused by structural or chemical defects that lead to an attenuation of the oscillatory PAC pattern. The parameter δ is the relative width of a Gaussian distribution.

Frequently, several fractions of nuclei with different QI's are found in the same compound. The effective perturbation is then given by

$$G_{kk}(t) = \sum_i f_i G_{kk}(t; \nu_{qi}, \eta_i, \delta_i), \quad (2)$$

where f_i (with $\sum_i f_i = 1$) is the relative intensity of the i th fraction with the QI parameters $\nu_{qi}, \eta_i, \delta_i$. These parameters and the intensities f_i were determined by least-squares fits of the theoretical perturbation factor Eq. (2) to the measured PAC spectra.

The experimental anisotropy at the time zero point is affected by prompt coincidences from the decay of the radioisotope ^{95}Zr produced by the neutron irradiation. Therefore the angular correlation coefficient A_{22} was fixed in the analysis for all temperatures to the value obtained from the fit to

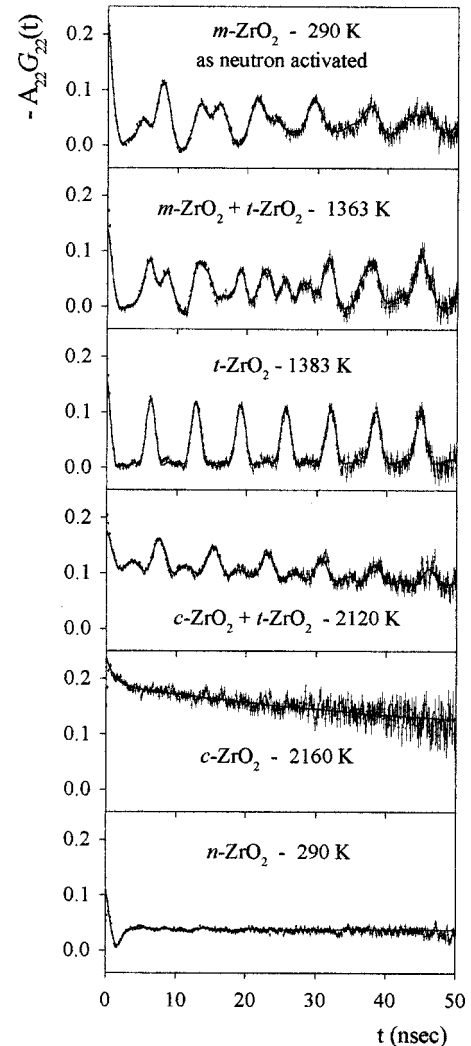


FIG. 3. PAC spectra of ^{181}Ta in coarse-grained ZrO_2 at different temperatures. For comparison, the bottom-most section shows the PAC spectrum of ^{181}Ta in noncoated nanocrystalline (n)- ZrO_2 at 290 K.

the spectrum with $T = 1500$ K. Because of the prompt contribution, only data points with delay times $t > 3$ ns were taken into account.

III. MEASUREMENTS AND RESULTS

Two different temperature programs were carried out for each of the two nanocrystalline compounds: In one series of measurements the temperature was continuously increased from 290 K up to $T \leq 1600$ K, in the other series the compounds were cycled through room temperature (RT), i.e., a PAC spectrum was taken at RT after each temperature increase between 290 and 1500 K. Typical data collection times for one spectrum were of the order of 15–20 h so that in both temperature programs the samples spent more or less the same time at a given temperature $T > 290$ K. Furthermore, these programs were applied to samples that had been annealed at 650 K for 24 h prior to the neutron irradiation (preannealing). In the case of noncoated n - ZrO_2 the rate of the $m \rightarrow t$ transformation at 1400 K was determined by a series of PAC measurements at subsequent times. Coarse-

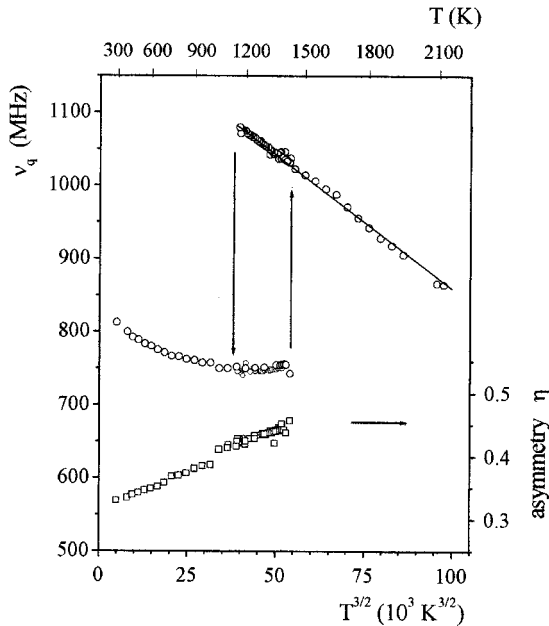


FIG. 4. The quadrupole frequency ν_q (open circles) and the asymmetry parameter η (open squares) of coarse-grained ZrO_2 vs temperature on a $T^{3/2}$ scale. The vertical arrows indicate the $m \rightarrow t$ and the reverse $t \rightarrow m$ transition, respectively, between the monoclinic and the tetragonal phase during heating and cooling, respectively.

grained ZrO_2 was investigated with particular emphasis on the monoclinic to tetragonal and the reverse tetragonal to monoclinic transformations by continuously heating and subsequent cooling in small steps.

A. ^{181}Ta PAC results for coarse-grained ZrO_2

Figure 3 shows typical PAC spectra of ^{181}Ta in coarse-grained ZrO_2 at different temperatures and illustrates that the three phases of ZrO_2 are easily identified by ^{181}Ta PAC spectroscopy: In the monoclinic phase the electric-field gradient is axially asymmetric and therefore gives rise to a nonperi-

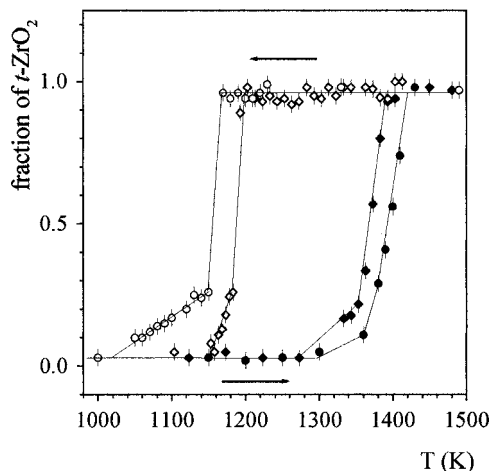


FIG. 5. The relative intensity of the tetragonal phase of two different samples (circles and diamonds, respectively) of coarse-grained ZrO_2 versus temperature. The full and open symbols show the tetragonal fraction during heating and cooling, respectively.

odic PAC pattern from which the quadrupole frequency ν_q , the asymmetry parameter η , and the relative width of the frequency distribution δ are readily deduced. The values for the RT spectrum in Fig. 3 are $\nu_q = 802(2)$ MHz, $\eta = 0.331(2)$, $\delta = 0.03(1)$, in agreement with previous investigations.^{7,8} The identification mark for the tetragonal phase is a periodic PAC pattern (see the 1383-K spectrum in Fig. 3) that reflects the axial symmetry ($\eta = 0$) of the EFG in this phase. At 1363 K the spectrum consists the superposition of a monoclinic and a tetragonal fraction, indicating that the $m \rightarrow t$ transition extends over a finite temperature range.

In perfect cubic symmetry the QI vanishes and the angular correlation is unperturbed, i.e., $G_{22}(t) = 1$. The PAC spectrum for perfect cubic symmetry therefore shows no modulation, but a constant anisotropy A_{22} independent of the time the nucleus has spent in the intermediate state of the cascade. Slight deviations from perfect cubic symmetry caused by defects, such as vacancies or impurities, may produce a small average EFG at the nuclear sites and lead to a weak decrease of the anisotropy with time. The spectrum observed at 2160 K shows this behavior and can therefore be associated with the cubic phase of ZrO_2 . The spectrum at 2120 K reveals a mixture of tetragonal and cubic ZrO_2 , indicating that the $t \rightarrow c$ transition also extends over a finite temperature range. For comparison with coarse-grained zirconia, the bottom-most section of Fig. 3 shows the spectrum of $n\text{-ZrO}_2$ for which electron diffraction⁴ indicates a cubic symmetry of the Zr lattice. Clearly, the PAC spectrum is strongly perturbed, reflecting the presence of strong QI's, which is incompatible with a cubic point symmetry at the probe site.

Figure 4 shows the temperature dependence of the quadrupole frequency ν_q and the asymmetry parameter η , Fig. 5 that of the fraction of tetragonal ZrO_2 . There is a hysteresis of the transition temperature between the monoclinic and the tetragonal phase as indicated by the arrows in Fig. 4, but the measured QI parameters are independent of the thermal history of the sample.

According to the PAC spectra in Fig. 3, the transition from the tetragonal to the cubic phase occurs around 2150 K. The temperature measurements in this range were carried out both with a W-Re thermocouple and a pyrometer, respectively. Both measurements agreed within 20 K.

B. ^{181}Ta PAC results for $n\text{-ZrO}_2$ and $n\text{-ZrO}_2/\text{Al}_2\text{O}_3$

Figure 6 shows typical examples of the ^{181}Ta PAC spectra observed in noncoated (left-hand side) and alumina-coated (right-hand side) $n\text{-ZrO}_2$, respectively, at 290 K after the neutron irradiation (top-most spectra) and at subsequently higher temperatures. These spectra were obtained with samples that had not been annealed prior to neutron irradiation and represent the series of measurements in which the temperature was continuously increased without cycling through 290 K.

The analysis of the spectra requires up to four different components with relative intensities $f_1 - f_4$. The spectra taken at RT after neutron activation show the typical features of a broad distribution of the QI and thus reflect a high degree of disorder, both for noncoated and coated ZrO_2 , respectively: From $G_{22}(0) = 1$ the perturbation factor passes through a minimum to an almost constant value (hard-core

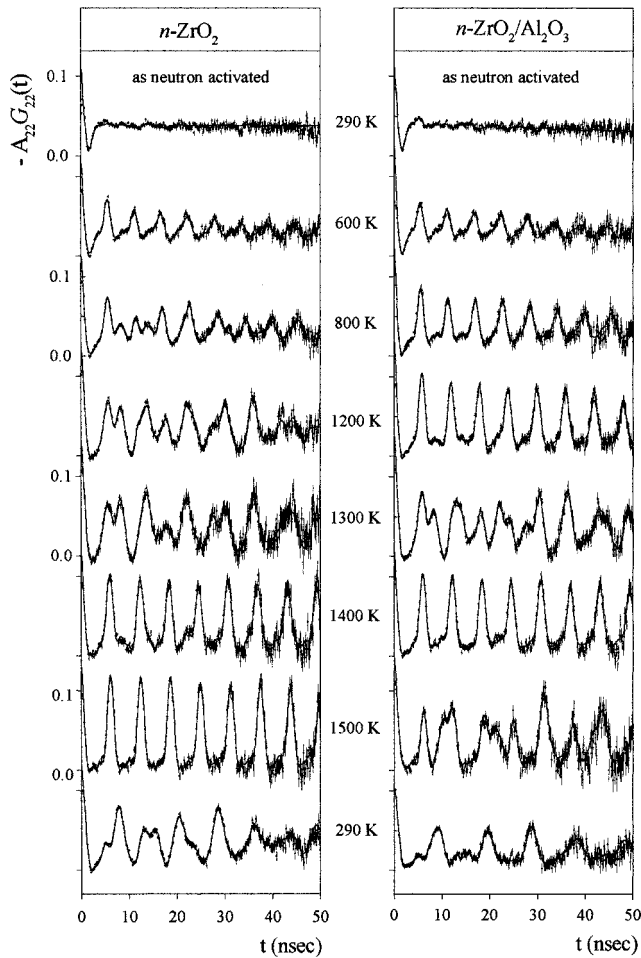


FIG. 6. PAC spectra of ^{181}Ta in noncoated $n\text{-ZrO}_2$ (left-hand column) and in Al_2O_3 -coated $n\text{-ZrO}_2$ (right-hand column) at different temperatures.

value¹⁷) at larger delay times with only slight indications of oscillatory components. The dominant component I (in the following denoted as disordered component) has a relative intensity $f_I \geq 0.85$ and QI parameters of $\nu_q \approx 1100$ MHz, $\eta \approx 0.6$ and $\delta \approx 0.35$. The weak oscillations superimposed on the hard-core value are best reproduced by admitting two further components with the parameters (II) $f_2 \leq 0.1$, $\nu_q \approx 780$ MHz, $\eta \approx 0.6$, and $\delta \approx 0.1$, and (III) $f_3 \leq 0.05$, $\nu_q \approx 1200$ MHz, $\eta \approx 0.2$, and $\delta \approx 0.05$. The QI parameters of components II and III, respectively, are close to those of monoclinic and tetragonal ZrO_2 , respectively. We may therefore conclude that after neutron irradiation the nanocrystalline samples contain less than 10% and 5%, respectively, of the ordered monoclinic and tetragonal phase of ZrO_2 , respectively.

Upon heating, a periodic, only weakly damped pattern appears from the RT spectrum (see the spectra at 600 K in Fig. 6), indicating the onset of an ordering process. The periodicity and the weak damping reflect an axially symmetric, well-defined QI. The quadrupole frequency is identical to that extrapolated from the high-temperature data of coarse-grained $t\text{-ZrO}_2$ (see Fig. 4). From the QI parameters ν_q , η and δ of the periodic pattern we may therefore conclude that the first ordered structure to emerge from the disorder at RT is the tetragonal phase, both in noncoated and coated

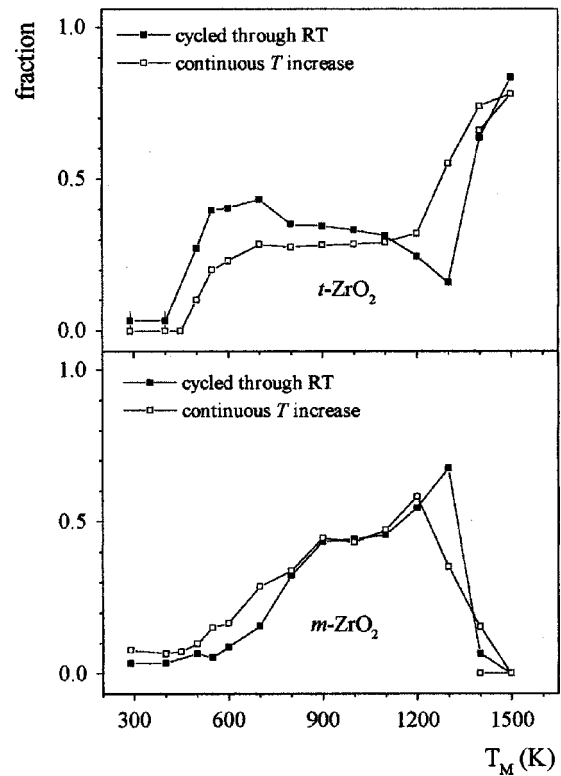


FIG. 7. The fractions of the monoclinic (lower section) and the tetragonal (upper section) phase in noncoated $n\text{-ZrO}_2$ at temperatures T_M for two different temperature programs: (i) continuously increasing temperature (open symbols) and (ii) cycling through RT after each temperature step (full symbols).

$n\text{-ZrO}_2$. The transformation of the disordered structure to the ordered tetragonal phase sets in rather abruptly at ~ 500 K in the case of a continuous temperature increase, and at a slightly higher temperature if the compound is cycled through RT.

A further component with well-defined QI parameters appears in noncoated $n\text{-ZrO}_2$ at ~ 700 K and in Al_2O_3 -coated $n\text{-ZrO}_2$ at 1300 K. From a comparison of its QI parameters with those of coarse-grained ZrO_2 (see Fig. 4), this third component can be identified as the ordered monoclinic phase of ZrO_2 . A fourth component with QI parameters $\nu_q \approx 600$ MHz, $\eta \leq 0.1$, and $\delta \approx 0.02$ was observed in coated $n\text{-ZrO}_2$ at $T \geq 1500$ K (see Fig. 6) and in noncoated $n\text{-ZrO}_2$ after cooling from 1500 K. This component persists when the samples are returned to RT [$\nu_q(290\text{ K}) \approx 660$ MHz] with the relative intensity depending on the thermal history. The QI parameters of this component, which—as shown by the small width of the frequency distribution—is well crystallized, are identical to those measured in natural and synthetic ZrSiO_4 .¹⁸ As the quartz tube started to flow around 1500 K, we therefore attribute this component to the formation of ZrSiO_4 by a $\text{SiO}_2\text{-ZrO}_2$ solid-state reaction. A $\text{Al}_2\text{O}_3\text{-ZrO}_2$ reaction can be excluded as this component appears both in coated and in noncoated $n\text{-ZrO}_2$.

Most spectra for $T \geq 1200$ K presented slight texture effects: The quality of the fits could usually be improved if the amplitudes s_{kn} in Eq. (1) were allowed to differ (by up to 20%) from the theoretical values for polycrystalline samples, which suggests the onset of particle growth at $T \sim 1200$ K.

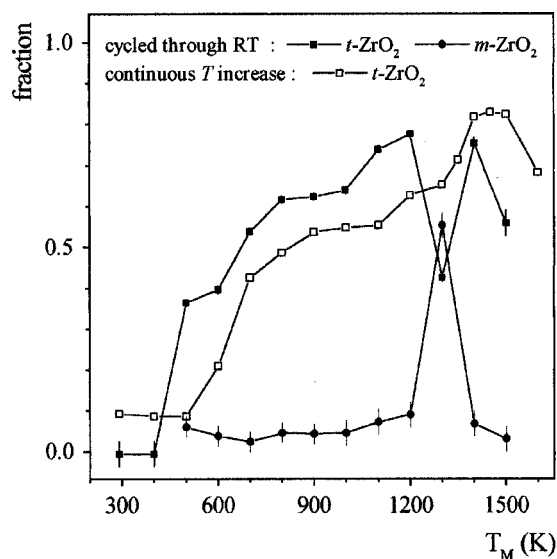


FIG. 8. The fractions of the monoclinic and the tetragonal phase in Al_2O_3 -coated $n\text{-ZrO}_2$ at temperatures T_M for two different temperature programs: (i) continuously increasing temperature (open symbols) and (ii) cycling through RT after each temperature step (full symbols). In the case of continuously increasing temperature the monoclinic phase is completely suppressed up to 1600 K.

The relative intensities or fractions of the ordered monoclinic and tetragonal phase of noncoated $n\text{-ZrO}_2$ and Al_2O_3 -coated $n\text{-ZrO}_2$, respectively, at temperatures T_M are collected in Figs. 7 and 8 for the two temperature programs: the open points were obtained by continuously increasing T_M from 290 to 1600 K, and the full points represent samples that were cycled through RT before each temperature increase. The fractions observed at RT as a function of the previous temperature value T_A (annealing temperature) are displayed in Fig. 9 both for noncoated and coated $n\text{-ZrO}_2$. For comparison, the previously reported T_A dependence of the RT fractions in a sample of $n\text{-ZrO}_2$ prepared by inert-gas condensation is included in Fig. 9 (bottom-most section).

The QI parameters ν_q , η , and δ determined in this study are collected in Figs. 10 and 11. Figure 10 compares the QI parameters of noncoated monoclinic $n\text{-ZrO}_2$ at 290 K after annealing at T_A for compounds prepared by plasma reaction⁴ and gas phase condensation,² respectively. The QI parameters of the monoclinic phase of noncoated $n\text{-ZrO}_2$ at temperature T_M agree within the errors with that of the coarse-grained compound (Fig. 4), and are therefore not shown. In $n\text{-ZrO}_2/\text{Al}_2\text{O}_3$ the monoclinic fraction is at most temperatures too small (see Figs. 8 and 9) for a precise determination of the QI parameters. The values at 1300 K $\nu_q(1300\text{ K}) = 745(2)$ MHz and $\eta(1300\text{ K}) = 0.435(3)$ are identical with those of coarse-grained $m\text{-ZrO}_2$ (see Fig. 4).

The QI parameters ν_q , η , and δ of the tetragonal component in coated and noncoated $n\text{-ZrO}_2$ as a function of T_M are collected in Fig. 11 for both temperature programs. For comparison, the temperature dependence of the quadrupole frequency of coarse-grained $t\text{-ZrO}_2$ (Fig. 4) is included. The QI parameters of the tetragonal phase at 290 K after annealing at T_A are independent of the thermal history and within the errors identical for coated and noncoated $n\text{-ZrO}_2$: $\nu_q(290\text{ K}) = 1225(6)$ MHz, $\eta(290\text{ K}) \leq 0.1$, and $\delta(290\text{ K}) \leq 0.02$.

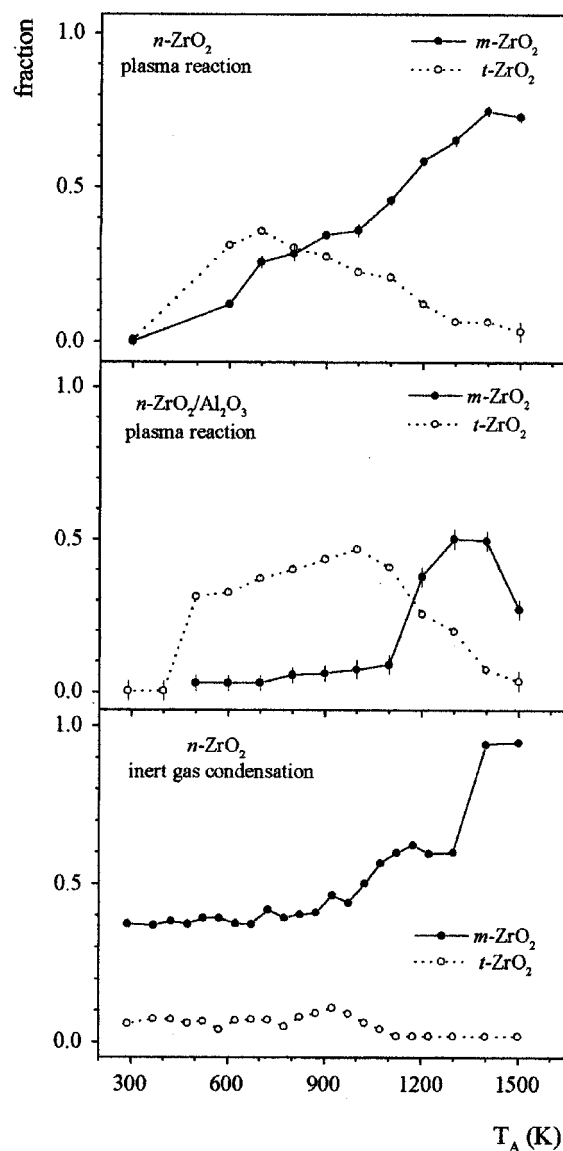


FIG. 9. The fractions of the monoclinic and the tetragonal (full and open circles, respectively) phase in $n\text{-ZrO}_2$ at 290 K vs. T_A of the previous temperature step. The fractions in noncoated and Al_2O_3 -coated $n\text{-ZrO}_2$ synthesized in a plasma reaction are compared to those in $n\text{-ZrO}_2$ produced by inert-gas condensation (bottom-most section).

C. The evolution of the phase equilibrium in $n\text{-ZrO}_2$ at 1400 K observed by PAC

In noncoated $n\text{-ZrO}_2$ the fraction of the monoclinic phase increases continuously up to $T \sim 1300$ K and then drops sharply, reflecting the transition to tetragonal $n\text{-ZrO}_2$ (see Fig. 7). We have investigated the evolution towards equilibrium of the tetragonal phase at 1400 K by PAC spectroscopy. For this purpose, a sample was kept at 1300 K for 24 h to reach equilibrium and then heated to 1400 K within a few minutes. At this temperature PAC spectra were recorded for fixed time intervals. Figure 12 shows the equilibrium spectrum at 1300 K and spectra after 3 and 12 h, respectively, at 1400 K. The spectra clearly evolve from the nonperiodic pattern characteristic for monoclinic ZrO_2 to the periodic pattern of tetragonal ZrO_2 . The growth of the tetragonal fraction with time from $f_t^0 \approx 0.3$ at 1300 K to the saturation value

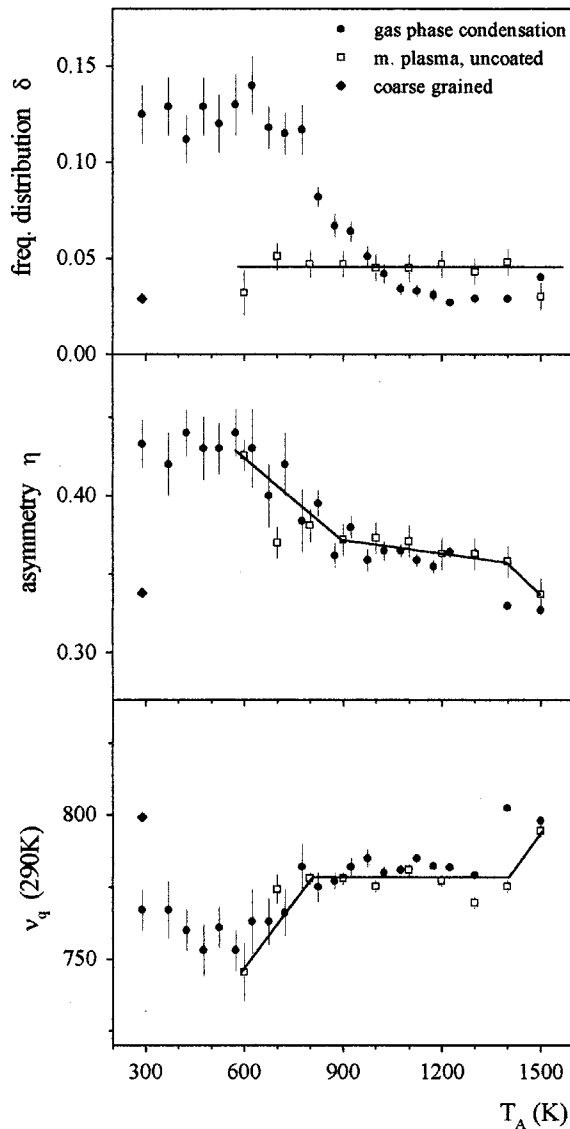


FIG. 10. The quadrupole frequency ν_q , the asymmetry parameter η , and the relative width δ of the Gaussian frequency distribution of the monoclinic phase at 290 K vs T_A of the previous temperature step for noncoated n -ZrO₂ prepared by gas phase condensation (full circles) and plasma reaction (open squares). The diamonds show the QI parameters of coarse-grained ZrO₂ at 290 K.

at 1400 K of $f_t^s \approx 0.8$ (full points in Fig. 13) and the corresponding decrease of the monoclinic fraction f_m (open points in Fig. 13) can be described by the relations $f_t(t) = f_t^0 + (f_t^s - f_t^0) [1 - \exp(-\lambda t)]$ and $f_m(t) = 1 - f_t(t)$, respectively, with a transformation rate of $\lambda = 6.9(1.2) \times 10^{-5} \text{ s}^{-1}$.

D. Search for recoil-induced radiation damage

The γ emission following the neutron capture in the activation process imparts a recoil on the PAC nucleus. In the case of ¹⁸¹Hf, the mother isotope of the PAC probe ¹⁸¹Ta, the maximum recoil energy is about 96 eV, which may be sufficient to displace the activated nucleus from its lattice position and produce a number of point defects near the PAC probe. Evidence for such recoil-induced defects has recently been reported by de la Presa and Lopez-Garcia¹⁹ for the per-

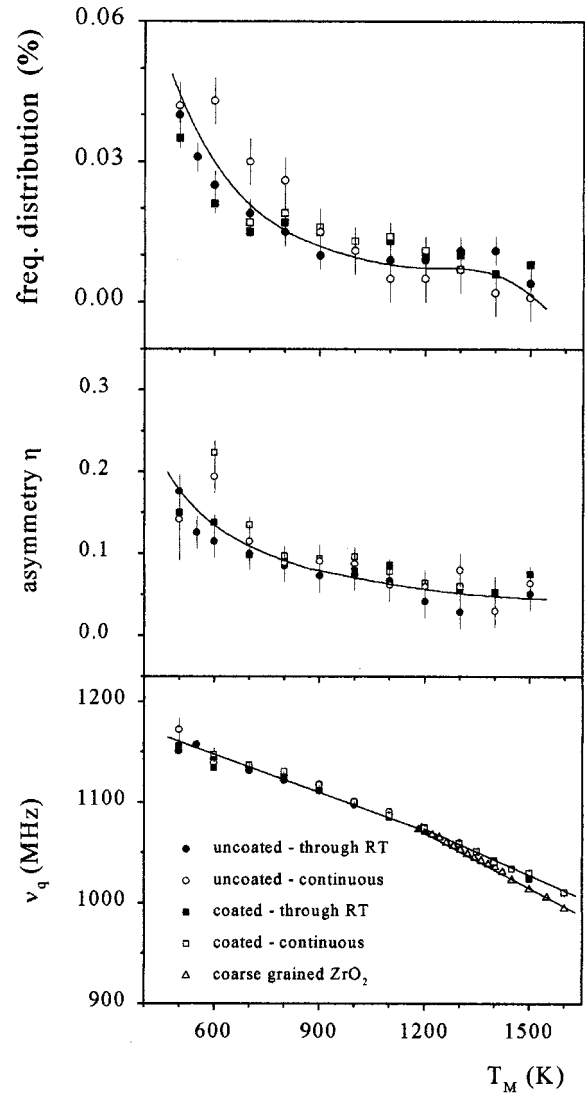


FIG. 11. The temperature dependence of quadrupole frequency ν_q , the asymmetry parameter η , and the relative width δ of the Gaussian frequency distribution of the tetragonal phase in coated and noncoated n -ZrO₂ for samples cycled through RT after each temperature step and continuously heated samples. For comparison, the quadrupole frequency of coarse-grained ZrO₂ is also shown.

ovskite CaHfO₃. It could therefore *a priori* not be excluded that the pronounced disorder in neutron-irradiated n -ZrO₂—as reflected by the broad frequency distribution of the PAC spectra at 290 K after activation—is caused by recoil-induced defects in the samples.

This question was investigated by annealing both coated and noncoated n -ZrO₂ at 650 K for 24 h prior to the neutron activation. As shown by the spectra in Fig. 6, annealing under these conditions produces a sizable fraction of ordered tetragonal ZrO₂. If recoil-induced radiation damage was important, one would expect a broad frequency distribution after activation both for the nonannealed and the preannealed material. The PAC spectra of the preannealed samples at 290 K, however, clearly showed the same periodic modulation of ordered t -ZrO₂ as the nonannealed material at 600 K (see Fig. 6). The pronounced disorder of the nonannealed samples

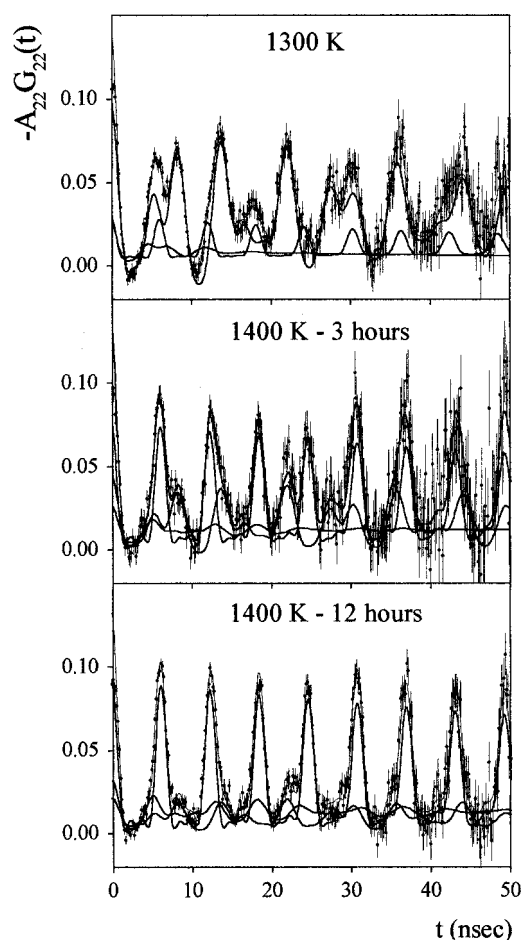


FIG. 12. PAC spectra of ^{181}Ta in $n\text{-ZrO}_2$ at 1300 K and after 3 and 12 h at 1400 K, respectively, illustrating the evolution towards phase equilibrium.

at 290 K is therefore inherent to the sample preparation and not the consequence of recoil-induced defects.

IV. DISCUSSION

A. Phase transitions in coarse-grained ZrO_2

The information on the $m \rightarrow t$ and the reverse $t \rightarrow m$ phase transformation obtained from the PAC spectra is collected in Fig. 5 where we have plotted the fraction of tetragonal ZrO_2 versus temperature for two compacted samples (diamonds and circles in Fig. 5) from the same lot of ZrO_2 . The full and open symbols refer to the fractions measured upon heating and cooling, respectively. For both samples the $m \rightarrow t$ transformation extends over a finite temperature range of about 50 K and there is some indication that about 50 K below the main transformation small amounts of $t\text{-ZrO}_2$ start to be formed. In contrast, the reverse $t \rightarrow m$ transition occurs very abruptly: at $T \sim 1170$ K 75% of the tetragonal phase transform to $m\text{-ZrO}_2$ within 10 K without any indication of a precursor formation of the m phase. The complete disappearance of the tetragonal phase, however, requires cooling of the two samples to 30 and 100 K, respectively, below the main transformation temperature. We also performed a few measurements with noncompacted ZrO_2 powder. The transitions were found to be similarly sharp, with the $m \rightarrow t$ trans-

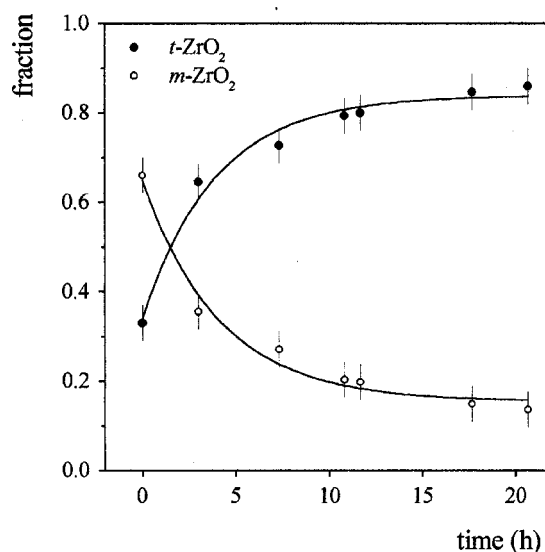


FIG. 13. The time dependence of the tetragonal fraction (full points) and the monoclinic fraction (open points) in $n\text{-ZrO}_2$ at 1400 K after rapid heating from 1300 K. The solid lines correspond to a $m \rightarrow t$ transformation rate of $\lambda = 6.9(1.2) \times 10^{-5} \text{ s}^{-1}$.

formation shifted by about 100 K to 1470 K and the $t \rightarrow m$ transition unshifted at 1170 K.

The hysteresis between the $m \rightarrow t$ and the $t \rightarrow m$ transformation for the two compacted samples shown in Fig. 5 is 180 and 240 K, respectively. With a third sample, which was not compacted to a pill, we found a hysteresis of 300 K, the same value as observed in the neutron-diffraction studies.^{21,22} It is well established²⁰ that the hysteresis increases with decreasing crystallite diameter. The different hysteresis values therefore probably reflect slight differences in the grain-size distribution of the samples, in part possibly caused by compacting the compounds to different extents.

In the qualitative characteristics of the transitions the PAC results agree with the conclusions from neutron-diffraction studies,^{21,22} in which the $m \rightarrow t$ transition was found to occur in two stages and to be less sharp than the reverse $t \rightarrow m$ transformation that had no m precursor, but indications of a t -post transformational stage. Quantitatively, however, the PAC and neutron-diffraction results differ considerably: In the neutron-diffraction study the diffuse $m \rightarrow t$ and the sharper $t \rightarrow m$ transformations extend over 600 and 150 K, respectively, transition ranges almost a factor of 10 larger than those deduced from the PAC spectra. The reasons for this pronounced difference are not clear. In addition to possible differences in the grain size, in impurity and oxygen vacancy concentration (the PAC samples were heated in a high vacuum, the neutron-diffraction samples in air) of the samples investigated by the two techniques, the fact that the PAC probe $^{181}\text{Hf}/^{181}\text{Ta}$ is an impurity in ZrO_2 may also be of importance: It is conceivable that the probe properties, in particular the larger mass, affect the transformation close to the probe site and as a short-sighted technique PAC samples the local probe environment rather than the averaged bulk properties as they are measured by neutron diffraction.

According to our measurements, the transition from the tetragonal to the cubic phase of ZrO_2 occurs around 2150 K. This value is 400 K lower than the temperature given in the literature for pure stoichiometric ZrO_2 . In substoichiometric

ZrO_{2-x}, however, the $t \rightarrow c$ transition temperature is predicted to decrease strongly with decreasing O/Zr ratio.^{23,24} As our samples were heated in vacuum, a certain O deficiency appears quite probable. In fact, the RT spectrum after 2160 K showed a considerably larger frequency distribution [$\delta=0.09(1)$] than the spectrum at the beginning of the study [$\delta=0.03(1)$], which points towards an increased concentration of defects such as oxygen vacancies. Again, the impurity nature of ¹⁸¹Hf/¹⁸¹Ta may also be of importance. It is well known²⁵ that impurities tend to stabilize the cubic phase of ZrO₂.

B. *n*-ZrO₂ and *n*-ZrO₂/Al₂O₃

1. Structural information on the as-prepared state

The PAC signal of the nanoscaled ZrO₂ compounds in the as-prepared state conveys the impression of an amorphous material: The spectrum is dominated by the disordered component that reflects a broad distribution of strong, axially asymmetric QI's. Recoil-induced radiation damage as a cause for the frequency distribution has been experimentally excluded. Furthermore, the disorder cannot be attributed exclusively to PAC probes situated in the crystallite interfaces because (i) in the as-prepared state practically all probes are subject to the QI distribution, the fraction of atoms located in the 1–2 outermost layers of a 5-nm crystallite, however, is of the order 40–70 % and (ii) a sizable ordered tetragonal component appears already at temperatures too low for significant crystal growth (see Figs. 7 and 8). This suggests that not only the PAC probes in the crystallite interfaces, but also those within the crystallites experience a disturbed local environment.

This conclusion from the PAC data appears to be in conflict with the electron-diffraction and electron-microscopy data since the electron diffraction and lattice imaging in the electron microscope indicate that the nanoscaled ZrO₂ particles crystallize in the cubic fluorite structure. For the PAC probes on Zr sites a cubic point symmetry, however, is incompatible with the observed QI distribution.

This impression of a conflict is the consequence of the different sensitivities of the two techniques: the electron methods display the long-range order of the Zr sublattice, while—because of the r^{-3} dependence of the EFG—the PAC method samples the charge distribution of the nearest-neighbor (NN) environment of the probe. In ZrO₂ the NN Zr-O interatomic distances are about 60% smaller than the Zr-Zr distances.²⁶ Therefore the QI of ¹⁸¹Ta on Zr sites is mainly determined by the oxygen environment and only minor contributions come from the Zr lattice. Consequently, the broad frequency distribution seen in the PAC spectra of the as-prepared specimens is equivalent to a wide distribution of the NN Zr-O distances.

Vacant oxygen sites caused by oxygen deficiency are probably one, but not the only, source of this disorder of the oxygen sublattice, because moderate annealing in vacuum is sufficient to produce a sizable well-ordered tetragonal component. Displacements of oxygen atoms from regular lattice, such as the partial occupation of the octahedral sites of the CaF₂ structure, has therefore to be considered as the other important source for the oxygen disorder. Slight strain-induced displacements of the Zr atoms from their regular

lattice sites (see Sec. II A and Ref. 27) may also contribute to the distribution of the Zr-O distances.

2. Phase transformations

The information obtained by this study on the phase transformations that occur upon heating is collected in Figs. 7 and 8 which show the temperature dependence of the fractions of monoclinic and tetragonal ZrO₂ in the nanoscaled particles. The transformation of the disordered component that characterizes the as-prepared state sets in at 500 K and it is the tetragonal phase that first emerges as a well-crystallized structure, both in *n*-ZrO₂ and *n*-ZrO₂/Al₂O₃, far below the $t \rightarrow m$ transition temperature of coarse-grained ZrO₂ (~1150 K, see Fig. 5).

In noncoated *n*-ZrO₂ (Fig. 7) the tetragonal phase grows rapidly to a relative intensity of ~50% at 600 K for samples cycled through RT and of ~30% when the temperature is continuously increased. At about 700 K the monoclinic phase starts to appear and its relative intensity increases continuously with temperature up to 1200 K. At $T_M > 1200$ K the fraction of the tetragonal phase increases strongly at the expense of the monoclinic phase, reflecting the $m \rightarrow t$ phase transition of ZrO₂. The decrease of the tetragonal fraction upon cooling from 1500 K reflects the onset of the solid-state reaction of ZrO₂ with the SiO₂ quartz capsule that produces the ZrSiO₄ component f_4 in the PAC spectra (see Sec. III B).

X-ray-diffraction⁵ studies of *n*-ZrO₂ synthesized by inert-gas condensation have established that the critical crystallite parameter to stabilize the tetragonal phase is of the order $d \leq 10$ nm which for this route of synthesis is reached at annealing temperatures of about 800–900 K. The continuous growth of the monoclinic fraction of plasma-produced noncoated *n*-ZrO₂ for $T_M > 700$ K (see Fig. 7) therefore probably reflects the growth of the particle size. It is, however, interesting to note that in the temperature interval of $T_M = 600$ –1200 K the tetragonal fraction remains more or less constant, which indicates that the transformation from the disordered structure to the tetragonal phase occurs with about the same rate as the tetragonal to monoclinic transformation.

In coated *n*-ZrO₂/Al₂O₃ (Fig. 8) the monoclinic phase is completely suppressed up to 1600 K, if the temperature is continuously raised. As the transformation from the tetragonal to the monoclinic phase is accompanied by a volume expansion of about 10%, the mechanical confinement of the *t*-ZrO₂ particles by the alumina coating produces compressive stresses which—as is well known—lead to a stabilization of the tetragonal phase. Furthermore, the Al₂O₃ coating can be expected to strongly hinder the particle growth, as ZrO₂ and Al₂O₃ are practically insoluble, which also contributes to the stabilization of the tetragonal phase up to 1600 K.

In samples of *n*-ZrO₂/Al₂O₃ cycled through RT the monoclinic fraction is less than 10% up to 1200 K and only at 1300 K the tetragonal phase becomes unstable and transforms to monoclinic ZrO₂. At slightly higher temperatures the monoclinic fraction disappears again because of the $m \rightarrow t$ phase transition that occurs between 1300 and 1400 K. Again, the ZrO₂-SiO₂ \rightarrow ZrSiO₄ reaction can be seen in the decrease of the tetragonal fraction from 1500 to 1600 K.

Figure 9 shows the fractions observed at RT as a function of the previous temperature value T_A both for noncoated and

coated n -ZrO₂, respectively. For comparison, the previously reported T_A dependence of the RT fractions of a sample of n -ZrO₂ prepared by inert-gas condensation is included (bottom-most section). The data in Fig. 9 have two interesting aspects:

First, one notes that the room-temperature stability of the ordered phases, as detected by the PAC spectroscopy, depends sensitively on the route of synthesis. In the gas phase condensation first nanoscaled Zr-metal particles are produced that are then oxidized, while in the plasma reaction ZrO₂ molecules are formed which then coalesce to nanoscaled particles. Figure 9 shows that the latter process results in a much higher annealing resistance and room-temperature stability of the tetragonal phase: Annealed n -ZrO₂ synthesized in a microwave plasma can contain about 50% of the well-ordered tetragonal phase at room temperature, whereas the relative intensity of the tetragonal phase in the RT PAC spectra of n -ZrO₂ produced by gas phase condensation is less than 10% after annealing up to 1200 K. This is probably a consequence of the different grain sizes: As the specimen of n -ZrO₂ produced by gas phase condensation had a larger average grain size than the material synthesized in the microwave plasma, the transformation from the ordered tetragonal to the monoclinic structure should be faster and therefore the amount of the tetragonal phase found at RT smaller.

The second interesting aspect in Fig. 9 is the observation that in n -ZrO₂/Al₂O₃—and to a lesser extent also in noncoated n -ZrO₂—the room-temperature fraction of the tetragonal phase $f_t(290\text{ K}; T_A)$ after annealing at $T_A \leq 1000\text{ K}$ is systematically smaller than the tetragonal fraction $f_t(T_M)$ measured at $T_M = T_A$ [e.g., $f_t(T_M = 800\text{ K}) = 0.62$, $f_t(290\text{ K}; T_A = 800\text{ K}) = 0.38$ in n -ZrO₂/Al₂O₃; compare Figs. 8 and 9]. For the monoclinic phase in n -ZrO₂, however, one finds $f_m(290\text{ K}; T_A) \approx f_m(T_A)$ (see Figs. 7 and 9).

Apparently, the well-ordered tetragonal component formed upon heating partially transforms back to the disordered phase when the compound is cooled to room temperature, while the monoclinic phase once formed remains stable upon cooling. This observation of a partially reversible disorder-order transformation is consistent with the fact that the micrographs remained unchanged upon annealing at 1100 K (see Sec. II A).

3. Quadrupole interaction parameters

The temperature dependence of the QI parameters ν_q and η of ¹⁸¹Ta in coarse-grained ZrO₂ is shown in Fig. 4. The data in Fig. 4 have been plotted on a $T^{3/2}$ scale, because in numerous metals and inorganic compounds the quadrupole frequency has been found to follow a $T^{3/2}$ dependence²⁸ $\nu_q(T) = \nu_q(0)(1 - BT^{3/2})$. While in the monoclinic phase the quadrupole frequency passes through a shallow minimum as one approaches the $m \rightarrow t$ transition, in the tetragonal phase it strongly decreases with increasing temperature. Between 1200 and 2100 K our data are well described by a $T^{3/2}$ relation with the parameters $\nu_q(0) = 1247(3)\text{ MHz}$ and $B = 3.1(1) \times 10^{-6}\text{ K}^{-3/2}$. Our results for ν_q and η in coarse-grained ZrO₂ confirm and extend the previous investigation by Jaeger *et al.*⁷ who studied the ¹⁸¹Ta QI in pure and yttria-stabilized zirconia up to 1750 K. A fit of the $T^{3/2}$ relation to the data of Jaeger *et al.*⁷ for pure ZrO₂ leads to the param-

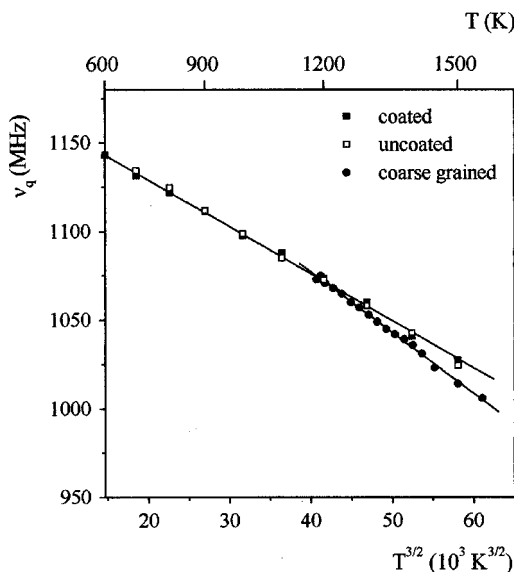


FIG. 14. The temperature dependence of quadrupole frequency ν_q in tetragonal ZrO₂ on a $T^{3/2}$ scale. Al₂O₃-coated and noncoated n -ZrO₂ (full and open squares) is compared to coarse-grained ZrO₂ (full points).

eters $\nu_q(0) = 1240(5)\text{ MHz}$ and $B = 2.9(1) \times 10^{-6}\text{ K}^{-3/2}$, in fair agreement with our result.

The QI parameters measured in n -ZrO₂ and n -ZrO₂/Al₂O₃ are shown in Figs. 10 and 11. Figure 10 displays the room-temperature values of ν_q , η , and δ after annealing at T_A for monoclinic n -ZrO₂ prepared by gas phase condensation and microwave plasma reaction. Both routes of synthesis lead to the same T_A dependence of the quadrupole frequency and the asymmetry parameter, which is discussed in detail in Ref. 2. The T_A dependence of the relative width δ of the frequency distribution, however, differs significantly for the two production methods: In n -ZrO₂ prepared by gas phase condensation the frequency distribution decreases with increasing annealing temperature towards the value of the coarse-grained compound that is reached at $T_A \geq 1000\text{ K}$, whereas in n -ZrO₂ produced in a plasma reaction the frequency distribution of the monoclinic fraction has the small width of the well-crystallized coarse-grained compound at its first appearance already.

The temperature dependence of the QI parameters of the tetragonal phase is shown in Fig. 11. Significant differences in the QI parameters of coated and noncoated tetragonal n -ZrO₂ are not observed. As indicated by the decrease of the relative width δ of the frequency distribution and of the asymmetry parameter η , both in coated and noncoated n -ZrO₂ the crystalline order increases with increasing temperature.

A very interesting aspect of the data in Fig. 11 is the observation that nanoscaled and coarse-grained ZrO₂ differ in the temperature dependence of the quadrupole frequency ν_q . This difference is illustrated by Fig. 14, where $\nu_q(T)$ of coated and noncoated n -ZrO₂ is compared to $\nu_q(T)$ of coarse-grained ZrO₂ on a $T^{3/2}$ scale. Clearly, in the entire temperature range $\nu_q(T)$ of n -ZrO₂ is well described by a $T^{3/2}$ relation. The parameters are $\nu_q(0) = 1188(5)\text{ MHz}$ and $B = 2.25(10) \times 10^{-6}\text{ K}^{-3/2}$: in n -ZrO₂ the strength parameter B is about 30% smaller than in coarse-grained ZrO₂ [B

$=3.1(1) \times 10^{-6} \text{ K}^{-3/2}$]. A similar observation was made in a recent PAC study of ZrO_2 -5 wt. % Al_2O_3 ceramics prepared by a precipitation method by Cervera *et al.*²⁹ For this compound with an initial crystallite diameter of the order of 10 nm the fit of a $T^{3/2}$ relation to the $\nu_q(T)$ data of the tetragonal phase gives the parameters $\nu_q(0) = 1169(10) \text{ MHz}$ and $B = 2.35(25) \times 10^{-6} \text{ K}^{-3/2}$.

The size dependence of the strength parameter B suggests an influence of the particle size on the phonon properties of ZrO_2 : Thermal vibrations of the host lattice atoms are generally considered as the main mechanism responsible for the temperature dependence of the QI in solids^{30,31} and the $T^{3/2}$ behavior is thought to reflect the temperature variation of the mean-square vibrational amplitudes of the host atoms. As at temperatures above the Debye temperature the mean-square vibrational amplitude is proportional to the inverse spring constant $(M\Theta_D^2)^{-1}$ of the lattice, with Θ_D the Debye temperature and M the atomic mass, Quitmann *et al.*³⁰ proposed the existence of a correlation $B \propto (M\Theta_D^2)^{-1}$ between the strength parameter and the inverse spring constant that could be experimentally confirmed by Mahnke *et al.*³²

With this picture of the temperature dependence of the QI, the smaller strength parameter in n - ZrO_2 points towards a decrease of the vibrational amplitudes or an increase of the Debye temperature $\Theta_D(n\text{-ZrO}_2) = 1.17(6) \Theta_D(cg\text{-ZrO}_2)$ relative to the coarse-grained (cg) material. An influence of the particle size on the phonon density of states has recently been observed in neutron scattering³³ and resonant inelastic nuclear γ -ray-scattering experiments.³⁴

V. CONCLUSIONS

In this paper we have reported perturbed-angular-correlation measurements of the electric quadrupole interac-

tion of the probe nucleus ^{181}Ta on Zr sites of Al_2O_3 -coated and noncoated nanometer-size (n) zirconia particles synthesized in a microwave plasma. For comparison, measurements of the ^{181}Ta QI in normal, coarse-grained zirconia were performed. These measurements complement the structural information on the nanoscaled particles obtained by electron-microscopy techniques and provide valuable insights into the effect of the particle size on the phase transformations of zirconia.

The main results may be summarized as follows: In the as-prepared state, the CaF_2 structure of the nanoscaled particles, both coated and noncoated, is characterized by an ordered cubic Zr and a highly disordered O sublattice. Upon annealing, the tetragonal phase is the first well-crystallized structure to emerge at about 500 K. This disorder-order transition connected with the cubic to tetragonal phase transformation is partially reversible upon cooling. In noncoated n - ZrO_2 the monoclinic (m) and the tetragonal (t) phase coexist in comparable fractions between at 600 K and the $m \rightarrow t$ transition temperature of coarse-grained zirconia at about 1300 K. In Al_2O_3 -coated n - ZrO_2 the monoclinic phase is completely suppressed up to 1600 K. This is attributed to the high hydrostatic pressure on the zirconia kernels resulting from the mechanical confinement by the alumina coating.

Both in nanoscaled and coarse-grained tetragonal ZrO_2 the ^{181}Ta quadrupole frequency ν_q shows a $T^{3/2}$ -temperature dependence. In the nanoscaled particles, however, the decrease of ν_q with increasing temperature is weaker than in the coarse-grained compound which suggests a decrease of the mean-square vibrational amplitudes with decreasing particle size.

ACKNOWLEDGMENTS

At the University of Bonn, this work has been supported by Deutsche Forschungsgemeinschaft, SFB 408.

-
- ¹H. Gleiter, *Prog. Mater. Sci.* **33**, 223 (1989).
²M. Forker, U. Brossmann, and R. Würschum, *Phys. Rev. B* **57**, 5177 (1998).
³D. Vollath and K. E. Sickafus, *Nanostruct. Mater.* **1**, 427 (1992); *J. Mater. Res.* **8**, 2978 (1993).
⁴D. Vollath and D. V. Szabo, *Nanostruct. Mater.* **4**, 927 (1994).
⁵R. Würschum, G. Soye, and H.-E. Schäfer, *Nanostruct. Mater.* **3**, 225 (1993).
⁶A. J. Allen, S. Krueger, G. G. Long, H. M. Kerch, H. Hahn, and G. Skanden, *Nanostruct. Mater.* **7**, 113 (1996).
⁷H. Jaeger, J. A. Gardner, J. C. Hygarth, and R. L. Rasera, *J. Am. Ceram. Soc.* **69**, 4589 (1986).
⁸A. Gardner, H. Jaeger, H. T. Su, W. H. Warnes, and J. C. Hygarth, *Physica B* **150**, 223 (1988).
⁹H. T. Su, R. Wang, H. Fuchs, J. A. Gardner, W. E. Evenson, and J. A. Sommers, *J. Am. Ceram. Soc.* **73**, 3215 (1990).
¹⁰M. C. Caracoche, P. C. Rivas, A. F. Pasquevich, A. R. Lopez-Garcia, E. F. Aglietti, and A. Scian, *J. Mater. Res.* **8**, 605 (1993).
¹¹R. Platzer, E. Karapetrova, M. O. Zacate, J. A. Gardner, J. A. Sommers, and W. E. Evenson, *Mater. Sci. Forum* **239-241**, 57 (1997).
¹²M. C. Caracoche, M. T. Dova, and A. R. Lopez-Garcia, *J. Mater. Res.* **5**, 1940 (1990).
¹³A. Scian, E. F. Aglietti, M. C. Caracoche, P. C. Rivas, A. F. Pasquevich, and A. R. Lopez-Garcia, *J. Am. Ceram. Soc.* **77**, 1525 (1994).
¹⁴P. C. Rivas, J. A. Martinez, M. C. Caracoche, A. Lopez-Garcia, L. C. Klein, and R. S. Pavlik, *J. Am. Ceram. Soc.* **78**, 1329 (1995). P. C. Rivas, M. C. Caracoche, J. A. Martinez, A. M. Rodriguez, R. Caruso, N. Pelligri, and O. de Sanctis, *J. Mater. Res.* **12**, 2594 (1997).
¹⁵U. Dehlinger and A. Kochendörfer, *Z. Kristallogr.* **101**, 134 (1939).
¹⁶M. Forker, W. Herz, U. Hütten, M. Müller, R. Müseler, J. Schmidberger, D. Simon, A. Weingarten, and S. C. Bedi, *Nucl. Instrum. Methods Phys. Res. A* **327**, 456 (1993).
¹⁷H. Frauenfelder and R. M. Steffen, in *Perturbed Angular Correlations*, edited by K. Karlsson, E. Matthias, and K. Siegbahn (North-Holland, Amsterdam, 1963).
¹⁸P. Lacentre and M. C. Caracoche, *Radiat. Eff. Defects Solids* **129**, 181 (1994); and M. C. Caracoche (private communication).
¹⁹P. de la Presa and A. Lopez-Garcia, *Radiat. Eff. Defects Solids* **140**, 141 (1997).
²⁰R. C. Garvie and M. F. Goss, *J. Mater. Sci.* **21**, 1253 (1986).
²¹F. Frey, H. Boysen, and T. Vogt, *Acta Crystallogr., Sect. B: Struct. Sci.* **46**, 724 (1990).

- ²²H. Boysen, F. Frey, and T. Vogt, *Acta Crystallogr., Sect. B: Struct. Sci.* **47**, 881 (1991).
- ²³R. J. Ackermann, S. P. Garg, and E. G. Rauh, *J. Am. Ceram. Soc.* **61**, 275 (1978).
- ²⁴P. Aldebert, J. M. Badie, J. P. Traverse, J. L. Buevoz, and G. Roul, *Acta Crystallogr., Sect. A: Cryst. Phys., Diffr., Theor. Gen. Crystallogr.* **31**, 239 (1975).
- ²⁵E. V. Stefanovich, A. L. Shluger, and C. R. A. Catlow, *Phys. Rev. B* **49**, 11 560 (1994).
- ²⁶R. Nitsche, M. Winterer, M. Croft, and H. Hahn, *Nucl. Instrum. Methods Phys. Res. B* **97**, 127 (1995).
- ²⁷R. Nitsche, M. Rodewald, G. Skandan, H. Fuess, and H. Hahn, *Nanostruct. Mater.* **7**, 535 (1996).
- ²⁸J. Christiansen, P. Heubes, R. Keitel, W. Loeffler, W. Sandner, and W. Witthuhn, *Z. Phys. B* **24**, 117 (1976).
- ²⁹M. M. Cervera, M. Escobar, M. C. Caracoche, P. C. Rivas, and A. M. Rodríguez, in *Proceedings of the 11th International Conference on Hyperfine Interactions, Durban, 1998* [Hyperfine Interact. **120-121**, 469 (1999)].
- ³⁰D. Quitmann, K. Nishiyama, and D. Riegel, in *Magnetic Resonance and Related Phenomena*, edited by P. S. Allen, E. R. Andrew, and C. A. Bates (North-Holland, Amsterdam, 1975).
- ³¹K. Nishiyama, F. Dimmling, Th. Kornrumpf, and D. Riegel, *Phys. Rev. Lett.* **37**, 357 (1976).
- ³²H. E. Mahnke, E. Dafni, M. H. Rafailovich, G. D. Sprouse, and E. Vapirev, *Phys. Lett.* **71A**, 112 (1979).
- ³³B. Fultz, J. L. Robertson, T. A. Stephens, L. J. Nagel, and S. Spooner, *J. Appl. Phys.* **79**, 8318 (1996).
- ³⁴B. Fultz, C. C. Ahn, E. E. Alp, W. Sturhahn, and T. S. Toeller, *Phys. Rev. Lett.* **79**, 937 (1997).